To appear in the *Journal of Geophysical Research*, 2001.

Local and remote atmospheric response to tropical instability waves: A global view from the space

Hiroshi Hashizume,[1] Shang-Ping Xie,[2] W. Timothy Liu,[3]
and Kensuke Takeuchi.[4]

Abstract

A La Niña took place in the equatorial Pacific in 1999, and strong tropical instability waves (TIWs) developed, causing large meanders of a sea surface temperature (SST) front between the equator and 3°N. High-resolution satellite measurements are used to describe the variability of SST, surface wind velocity, column-integrated water vapor, cloud liquid water and precipitation associated with these strong TIWs in 1999. Coherent ocean-atmosphere patterns emerge in both the Pacific and Atlantic, revealing rich regional characteristics. In the far eastern Pacific, southeasterly trades strengthen (weaken) over positive (negative) SST anomalies, apparently due to enhanced (reduced) mixing with high-speed winds aloft. In the central Pacific, we find evidence that SST-induced sea level pressure changes also contribute substantially to wind fluctuations. Similar SST-wind co-variability also exists in the Southern Hemisphere along 2°S, but the wind variability induced by unit SST anomaly is much larger than that north of the equator. In the central Pacific where the equatorial front is broad, the northern SST pattern has a large meridional scale and reaches as far north as 6°N. Further to the north in the intertropical convergence zone (ITCZ) where local SST anomalies are small, significant variability is found in clouds and precipitation, which is further correlated with surface wind convergence. In the Atlantic, TIW signals in SST are strongly trapped near the equator, but they induce significant remote response in the ITCZ, which takes a more southern position than its Pacific counterpart and thus more susceptible to TIW influence.

1. Introduction

Cusp-shaped frontal waves are often observed in the second half of a year in the eastern Pacific north of the equator [*Legeckis,* 1977], where a strong sea surface temperature (SST) front separates cold upwelled water on the equator from warmer surface water that supports the intertropical convergence zone (ITCZ) further to the north. Figure 1 is a snapshot of tropical instability waves (TIWs). They typically have a wavelength of 1000 km, a period of 30 days and a westward phase speed of 0.4 m/s. These numbers can vary by as much as 20%-30%, both interannually and among individual waves.

The cause of TIWs is generally attributed to hydrodynamic instability of shears associated with strong equatorial currents flowing in alternating directions [*Philander,* 1978; *Cox,* 1980]. Observations confirm that these TIWs act to reduce the shears of mean oceanic currents [*Weisberg,* 1984; *Hansen and Paul,* 1984]. Recent theoretical studies suggest that the strong temperature gradients in the mixed layer can also contribute significantly to developing TIWs [*Yu et al.,* 1995]. TIWs have a distinctive seasonal cycle. Generally, these SST frontal waves begin to be visible in June and decay as the new year starts.

Whereas TIWs have oceanic origin, the induced SST variations are 2°-3°C in magnitude and can induce atmospheric variability. The first indication of possible co-variability in surface wind was in *Halpern et al.* [1988] who found a peak in meridional wind velocity spectra–albeit weak and not statistically significant–at the frequency of TIWs at equatorial mooring sites at 110°W and 124°W. Using the space difference as a high-pass filter, *Hayes et al.* [1989] showed that surface wind velocity at 110°W was statistically significantly correlated with local SST, thus establishing the existence of atmospheric co-variability with oceanic TIWs. *Deser et al.* [1993] show that low-level clouds tend to form over the troughs of the SST waves while clear sky conditions tend to prevail over the ridges. The altitude of the cloud top is not determined, but this association of clouds and TIWs indicate that the atmospheric response is not confined to the surface but extends over a certain depth.

The advent of satellite scatterometer revolutionized the practice of surface wind observation [e.g., *Liu et al.,* 1998], which had to rely on sparse ship, buoy and island measurements. Using measurements by the European Remote-sensing Satellite 1 (ERS-1), *Xie et al.* [1998] demonstrate satellite scatterometer's ability in capturing TIW-induced wind fluctuations and obtain a horizontal map of the SST-wind covariability that is consistent with *Hayes et al.* [1989]. *Hashizume* [1998] obtain similar results by applying the cross-correlation analysis to the NASA's Scatterometer (NSCAT) data, which are of higher space-time resolutions but cover only a portion of the 1996 TIW-active season. He further detects a weak signal in column-integrated water vapor content in the Special Sensor Microwave/Imager (SSM/I) measurements and relates it to scatterometer-derived surface wind convergence. *Liu et al.* [2000] examined the variation of surface wind vector, SST and column-integrated water vapor content associated with TIW, using new and better sampled spacebased observations.

Within the equatorial cold tongue, the southeasterly wind speed increases with height in the atmospheric planetary boundary layer (PBL), and this strong vertical shear is the major source of turbulence in this region where a temperature inversion caps the PBL. Over warm SST regions north of the SST front, reduced static stability intensifies vertical mixing, which in turn accelerates the southeasterly winds at the surface [*Wallace et al.,* 1989]. *Hayes et al.'s* [1989] analysis of moored buoy data at 110°W supports this vertical momentum mixing mechanism. Results from a global general circulation model (GCM) also confirm that vertical viscosity increases by one order of magnitude over the troughs of SST waves [*Xie et al.,* 1998]. Given that the atmospheric response extends to certain height from the sea surface as indicated by the cloud co-variability, SST-induced air temperature anomalies can change sea level pressure (SLP; *Lindzen and Nigam* [1987]) and contribute to wind variability. Thus, SLP-induced wind variability is 90° out of phase with the SST anomaly, while the vertical mixing mechanism induces wind anomalies that are in phase with local SST variations. This difference between the SLP and vertical mixing mechanisms allows *Hayes et al.* [1989] to infer the their relative importance by analyzing the zonal phase of wind anomalies relative to SST ones. We will use the same methodology here.

Similarly, two independent mechanisms have been proposed for the low-level cloud pattern. *Deser et al.* [1993] propose that as the southeasterly trades blow across the meandering equatorial front, thermal convection may occur over the warm sector and help form clouds. *Xie et al.'s* [1998] GCM results sug-

gest an alternative mechanism, in which perturbation wind convergence favors cloud formation by increasing humidity near the PBL top. If easterly wind and SST anomalies are in phase, cloud cover anomalies due to this vertical advection mechanism are 90° out of phase with those due to *Deser et al.'s* convective mechanism.

A weak La Niña took place in the equatorial Pacific in 1999, where SSTs were 1°C below the normal in the east. TIWs started to develop in May in the east, grew into large amplitudes and remained strong as the year ended. Coinciding with the developing TIWs, NASA's QuikSCAT satellite was launched into the space in June, and its scatterometer SeaWinds offers a high-resolution, nearly global view of the world ocean on a daily basis [*Liu et al.,* 2000]. In addition, the co-orbiting Tropical Rain Measuring Mission (TRMM) Microwave Imager (TMI) provides tropical SST fields nearly free of contamination of clouds [*Wentz et al.,* 2000; *Chelton et al.,* 2000a]. Exceptionally strong TIWs and this suite of new satellites that observed these waves make the year of 1999 an unprecedented opportunity to study the coupled aspect of TIWs. Using QuikSCAT and TMI data, *Liu et al.* [2000] examined the phase difference between SST and wind components of TIW, and *Chelton et al.* [2000b] found a linear relationship between the wind convergence (curl) and downwind (crosswind) SST gradient. Both studies confirm the vertical mixing mechanism of *Wallace et al.* [1989] and *Hayes et al.* [1989].

Here we use these new satellite measurements to map the spatial structures of ocean-atmosphere variability in SST, surface wind, water vapor, clouds and precipitation associated with the 1999 TIWs. We will base our discussion mostly on regression analysis onto the SST time series at a reference station. By changing this reference station, we can obtain maps of the ocean-atmosphere co-variability associated with TIWs in different regions. The mean state of the PBL varies considerably between 90°W to 180°, a longitudinal band where energetic TIWs are observed. For example, surface winds change from nearly southerly at 90°W to nearly easterly at 180°, while equatorial SSTs increase by 7°C (Figure 2). Such large changes in the mean state can affect the relative importance of various mechanisms and the regional characters revealed by these regression maps can give us further insights on how these mechanisms operate. Particularly, we would like to address the following questions. Given that the atmospheric variability penetrates a certain depth, is there any evidence for SST-induced SLP mechanism for wind variability? Given TIW-induced wind convergence observed by ERS-1 [*Xie et al.,* 1998], can we see its effect on moisture and cloud fields?

The rest of the paper is organized as follows. Section 2 describes the data and analysis procedures. Sections 3 and 4 present results for the Pacific and Atlantic, respectively. Section 5 is a summary.

2. Data and methodology

We use the TMI SST product, which unlike satellite infrared radiometers, is much less contaminated by clouds. TMI/SST sensing fails only in the presence of strong precipitating clouds [*Shibata et al.,* 1999]. The TMI also measures column-integrated water vapor (WV), cloud liquid water (LW) and precipitation [*Wentz,* 1997]. Dominated by high-frequency weathers, these hydrological variables are poorly sampled by a single microwave imager. We thus combine the TMI and three SSM/Is (F-11, F-13 and F-14) that were in space simultaneously with the TRMM. This combination of four microwave imagers greatly improves the sampling of WV, LW and precipitation. The TMI and SSM/I data are originally gridded at a $0.25° \times 0.25°$ and twice daily resolution by Remote Sensing Systems. An enhanced dataset is generated by combining the measurements on these four co-orbiting satellites; we average all the measurements for an interval of three days at a given grid point.

Compared to other previous scatterometers, the SeaWinds on the QuikSCAT satellite significantly improves the space-time resolution of satellite-based surface wind measurements, providing a daily coverage over 90% of the global ocean. We use the SeaWinds data product interpolated by a successive correction method [*Liu et al.,* 1998] to daily $0.5° \times 0.5°$ grid fields. To be consistent with the TMI-SSM/I dataset, we use a three-day average wind vector dataset in the subsequent analysis. The combined TMI-SSM/I data are re-gridded onto the same $0.5° \times 0.5°$ grid as the SeaWinds dataset by averaging on neighboring grid points. The SeaWinds data are available from July 21, 1999. Unless stated otherwise, our analysis covers a five-month period from July 21 to December 28, 1999, which saw five TIWs at a given grid point in the eastern Pacific.

The Pacific TIWs have a typical wavelength slightly longer than 10° in longitude in 1999. We apply a spatial filter of 12° moving average in the zonal

direction, which works well in removing the slow-varying basin-scale mean state and extracting the TIW signals. Even without any temporal filtering, TIW signals in SST, wind velocity, LW and WV are clearly visible in longitude-time sections (Figure 3). The co-propagation of theses ocean-atmospheric variables is very unlikely to be due to satellite track and sampling problems as these data are derived from five independent satellites. Slight changes in the moving average window do not affect subsequent results.

We will use the linear regression technique to map the spatial structure of coupled TIWs, where we seek a linear relation between, say zonal wind velocity $U(x, y, t)$ and SST at a reference station $T(t)$:

$$U = aT. \tag{1}$$

A least-square fitting leads to the regression coefficient,

$$a(x, y) = \sum_{n=1}^{N} U(x, y, t_n)T(t_n) / \sum_{n=1}^{N} T^2(t_n). \tag{2}$$

This regression technique is suitable for extracting regional characters compared to other global analysis techniques such as Empirical Orthogonal Function (EOF). Because SSTs vary on much slower time scales than other variables, we will regress two-dimensional fields onto the SST time series on a chosen grid point referred to hereafter as the center point. We will further compute the regression functions based on SST time series at all grid points within a 5° range both to the west and east, and construct a composite map by averaging these regression functions–21 in total–while matching the reference to the center point. This composite procedure reduces the noises in a single regression map considerably, although the latter can still capture the gross TIW structures (not shown). Spatially filtered SSTs are not completely free of high- and low-frequency perturbations irrelevant to TIWs. To remove these noises, we apply a band-pass filter to the reference SST time series by subtracting 11-point from 3-point running averages. This band-pass filter slightly improves the regression maps, but does not change the results to be presented in any significant way.

3. Pacific variability

Figure 2a shows the variance of spatially filtered SST anomalies along with time-mean SSTs. Largest variance is found north of the equator where there are high meridional SST gradients. TIWs grow from the Galapagos westward, reach maximum amplitudes around 120°W, and then reduce their variance farther to the west. There is also a tendency for the latitude of maximum variance to shift slightly northward, from 1°N at 100°W to 4°N at 170°W. The equator appears as a zone of minimum TIW variance. There is a weak secondary maximum narrowly centered at 2°S. This equatorial asymmetry in TIW activity results from the asymmetry in the annual-mean climate in the eastern Pacific that involves ocean-atmosphere interaction of a different kind (see *Xie* [1996] for a review of this climatic problem). TIWs transport heat northward [e.g., *Hansen and Paul,* 1984] and may contribute to the broadening of high SST gradient zone north of the equator from the Galapagos westward. Accordingly, TIWs are more confined near the equator in the east than further to the west. In the remaining part of the paper, we will present regression maps and investigate how the large zonal variations in the mean state might affect the characteristics of TIWs in the ocean and atmosphere.

3.1. Far eastern Pacific (105°W)

In the far eastern Pacific, the maximum TIW amplitude is located around 1°N. Figure 4 are the composite regression maps with the center point at 105°W, 1°N. SST anomalies are largely confined between the equator and 3°N, where strong meridional gradients in the mean SST are found. Perturbation winds have a strong meridional component and tend to enhance (reduce) the prevailing southeasterlies over positive (negative) SST anomalies. This wind response appears to be dominated by local vertical mixing adjustment, with both its phase and amplitude proportional to those of local SST anomalies. This wind anomaly pattern is similar to what *Hayes et al.* [1989] inferred from near-equatorial mooring observations at 110°W. North of 3°N, SST variations become weak but show a northeastward phase tilt that is typical of TIWs. Wind anomalies are weak accordingly and their phase tends to become in quadrature with SST's, a change that seems indicative of the Lindzen-Nigam SLP mechanism. We will return to this point later.

Our regression analysis captures clear signals in WV and LW, whose statistical significance is visually apparent in their westward co-propagation with SST and wind speed in longitude-time sections (Figure 3). Both local SST and wind convergence affect WV; Enhanced turbulence over a warm SST can mix

moist air upward while surface wind convergence increases moisture in the PBL. Between the equator and 1°N, anomalous winds are divergent (convergent) over positive (negative) SST anomalies. Because of the opposing effects of local SST and moisture convergence, WV signal is weak there. At 2°N where SST and wind convergence are in phase, WV reaches a maximum. Further north, SST anomalies become small and wind convergence becomes the dominant mechanism for WV variations, which show a slight northwestward phase tilt in contrast to SST's northeastward tilt. The general tendency for large WV anomalies to be located north of SST ones may reflect the northward increasing trend of the mean SST and WV; Unit wind convergence over warmer SSTs can generate stronger moisture convergence. Significant wind divergence anomalies are present south of the equator (Figure 4c), but WV signals are weak there presumably because of the small mean moisture content and a shallow PBL.

LW variability is confined in a narrow latitudinal band between 1°N and 3°N, and appears associated with non-precipitating low-level clouds. No significant rainfall is detected over major LW anomaly centers at 2°N. This collocation of SST troughs and clouds is first reported by *Deser et al.* [1993]. The mean-LW plateau between 1°N and 3°N is a signature of these low-level clouds that are accompanied by little precipitation (Figure 5a). *Deser et al.* suggest that these low clouds are due to thermal convection associated with cold air advection from the equator. Because SST and wind convergence are in phase at 2°N, it is hard to tell whether SST-induced mixing or convergence is more important. A general tendency for LW's phase to shift slightly eastward relative to SST's seems to support *Deser et al.'s* hypothesis that cloud variability is caused by advection across strong SST gradients. The maximum regression coefficient for LW is about 10% of the mean and 30% of the total root mean square (RMS) variance (Figures 5a and 5c).

3.2. Central Pacific (125°W)

Further to the west, the maximum TIW variance shifts to 2°N. Figure 6a shows the regression map centered at 125°W, 2°N. The SST pattern has a considerably broader meridional scale than at 105°W, consistent with the variance distribution in Figure 2. This increase of meridional scale is particularly clear in wind variability. Another notable difference from the 105°W map is that zonal wind anomalies are dominant at 125°W.

Significant SST anomalies appear also south of the equator, centered at 2°S with opposite signs to those to the north. Large wind variability, almost as large as north of the equator, is associated with those southern SST anomalies. Such coherent SST-wind patterns in association with TIWs in the Southern Hemisphere are reported in *Xie et al.'s* [1998] analysis of ERS-1 data. TIW signals in sea level height south of the equator is recently documented by *Chelton et al.* [2000c] using satellite altimetry measurements.

Figure 7 shows scatter plots of SST and wind speed anomalies for 2°N and 2°S. The slopes of these scatters are significantly different north and south of the equator. The 140°W-110°W mean regression coefficient for wind speed is 1.83 (0.64) $\mathrm{ms}^{-1}\mathrm{K}^{-1}$ at 2°S (2°N). Thus, unit SST change induces nearly three times as large wind anomalies south as that north of the equator. Lower SST, more stable stratification, and hence stronger vertical wind shear in the mean state may contribute to this stronger coupling between the SST and wind variability south of the equator. An alternative explanation has to do with a negative feedback between wind speed and SST; Intensified winds over warm SSTs act to dampen the SST anomalies via latent and sensible heat flux. This negative feedback affects the wind/SST ratio and may cause its apparent difference across the equator.

A close examination of SST-wind co-variability patterns indicates that wind regression is not perfectly in phase with SST as in the far eastern Pacific, but their phases shift in a systematic way consistent with the SST-induced SLP mechanism. This is especially obvious along the equator, where SST anomalies virtually vanish but significant meridional winds are observed crossing the equator from the cold to warm SST center. Here we use a crude method to separate the wind anomalies due to vertical mixing from those due to SLP gradient. We assume that vertical mixing is strong in the near-surface boundary layer so that the adjustment to an anomalous change in SST is completed instantaneously and the wind response so induced is correlated with the local SST anomalies. This quasi-steady local adjustment assumption appears to be valid, and horizontal advective effects seem small given that SST and wind anomalies are roughly in phase in the far eastern Pacific (Figure 4). We first perform a least-square fit of wind velocity and SST at each latitude in the zonal direction for 135°W-115°W and attribute the wind anomalies ($\boldsymbol{U_m}$) explained by this local spatial correlation to

vertical mixing mechanism

$$\boldsymbol{U_m} = \boldsymbol{A}(y)T(x,y), \tag{3}$$

where $\boldsymbol{A} = (A_u, A_v)$ are respectively the regression coefficients for zonal and meridional wind components and vary with latitude, and T is the composite regression pattern based on the SST time series at 125°W, 2°N. Deriving regression relation separately for zonal and meridional wind velocity seems justified because they are governed by different dynamics near the equator; The zonal wind velocity is nearly in geostrophic balance while meridional wind in the PBL is largely driven by surface friction and SST gradient [*Lindzen and Nigam,* 1987]. A more rigorous justification for separate regression equations, however, requires the knowledge of vertical wind structure.

The middle panel of Figure 6 shows the regression for zonal wind component from this least-square fit. The much larger regression coefficient south than north of the equator can be seen again here. The right panel shows the residual, $\boldsymbol{U_p} = \boldsymbol{U} - \boldsymbol{U_m}$, which may be attributed to mechanisms other than local vertical mixing adjustment. The $\boldsymbol{U_p}$ map indicates that the residual wind velocity south of 4°N is consistent with the SLP mechanism, flowing from cold to warm ocean surface. The magnitudes of $\boldsymbol{U_p}$ and $\boldsymbol{U_m}$ are comparable in this longitudinal sector. When the same analysis is applied to the 105°W regression pattern, $\boldsymbol{U_p}$ is still consistent with the SST/SLP mechanism but its magnitude is only one third of $\boldsymbol{U_m}$ (not shown). This regional difference in atmospheric response explains why *Hayes et al.* [1989] did not find evidence for SLP-driven wind anomalies at 110°W.

Although SST anomalies (SSTAs) at 2°N are more than twice as large as at 2°S, $\boldsymbol{U_p}$ is comparable in magnitude north and south of the equator. Stronger vertical mixing and dissipation in the mean state at 2°N can cause this asymmetry in the $\boldsymbol{U_p}$/SSTA ratio, or alternatively, unit SSTA induces a larger SLP anomaly south than north of the equator for some unknown reasons. North of 4°N, $\boldsymbol{U_p}$ directs from warm to cold sea surface and cannot be explained by local SST-induced SLP anomalies. The $\boldsymbol{U_m}$/SSTA ratio reaches a local maximum at 4°N, which is twice as large as at 2°N. It remained to be sorted out what causes this meridional variation in the $\boldsymbol{U_m}$/SSTA ratio, and what causes the wind north of 4°N to deviate from the local mixing adjustment.

The regression patterns for WV, LW, and rain are similar to those at 135°W, 5°N, which will be presented shown in the next subsection.

3.3. Influences on the ITCZ

Based on a GCM simulation, *Xie et al.* [1998] suggest that TIWs may induce remote response in the atmosphere and affect the ITCZ that is not under the direct forcing of SST waves. Here we use the high-resolution satellite data to test this hypothesis and to detect convective signals in the ITCZ. Interested in signals farther north, we choose 135°W, 5°N as the center point for the regression analysis because it has reasonably large SST variance (RMS = 0.5°C) and is close to the ITCZ whose southern boundary is found at 7°N at this longitude (Figure 2b).

Figure 8 shows the regression maps. Although SST anomalies vanish at about 7°N, significant wind anomalies remain as far north as 10°N. Wind velocity pattern is dominated by local processes such as vertical mixing and SST-induced SLP changes south of 6°N as discussed in previous subsections, but its mechanism becomes less clear further north. Regardless of the mechanism, meridional wind velocity north of 7°N is very robust, in quadrature with SST and southerly (northerly) in the present of an eastward (westward) SST gradient to the south at 6°N. Despite a lack of local SST anomalies, this meridional wind signal appears to be statistically significant judging from the repetition of this pattern in the zonal direction. It is also interesting to note that north of 6°N, anomalous winds start to show a rotational tendency, maybe indicative of the influence of the earth rotation.

Unlike the 105°W map where maximum TIW amplitudes are found far south of the ITCZ, there are large anomaly centers along 6°N-7°N in the WV regression for 135°W. These WV anomalies are clearly associated with low-level wind convergence, but are nearly in quadrature with SSTAs at 6°N. More importantly, they are part of the ITCZ variability that includes cloud liquid water and precipitation. The statistic significance for anomalies north of 8°N is hard to judge, but anomalies between 5°N-8°N are robust and show consistent correspondence to each of the SST waves. The axis of these anomaly centers tilts slightly toward the northeast, in the direction the mean ITCZ slants. Figure 5d shows the standard deviation of intra-monthly variability in ITCZ precipitation and LW. The maximum precipitation regression is about 15-20% of the total RMS variance of the ITCZ, a quite large number considering the center of TIW-induced SST variability is located further south. The precipitation signal indicates that the remote response in the ITCZ may have a deep vertical

structure extending beyond the PBL top.

Independent of TIWs, synoptic disturbances of a typical zonal wavelength of 50° and time scale of a week is known to exist near the eastern Pacific ITCZ and propagate westward or northwestward [*Chang,* 1971; *Lau and Lau,* 1990; *Raymond et al.,* 1998]. Maps of hydrological variables–WV, LW and precipitation–based on raw satellite data are dominated by these synoptic disturbances (not shown). Fortunately, because of a good scale-separation between synoptic waves and TIWs, our spatial filter successfully removes most of the former without losing much of the TIW signals. Figure 9 shows longitude-time sections of spatially filtered SST at 4°N, LW and WV for 6°N-7°N. Even without further temporal filtering, TIW-induced LW and WV signals–though much noisier than wind speed–are visible within the ITCZ, propagating westward with the SST waves. This visual examination reinforces the statistic significance of ITCZ variability remotely forced by TIWs. We also carried out regression analysis for the first and second 2.5-month sub-periods separately, and the regression maps for each sub-period (not shown) looked very similar to Figure 8.

Significant features also appear in WV and LW at lower latitudes (Figure 8). WV is more closely in phase with SST immediately north of the equator, but their phase difference increases as we move either further north or cross the equator into the Southern Hemisphere, indicative of increasing contribution from surface wind convergence. WV and SST become almost in quadrature at 6°N and 2°S. The LW anomaly centers along 3°N are roughly in phase with SSTAs and shift to east of WV centers. It is interesting to note that these non-precipitating cloud patterns decay westward and become very weak west of 135°W, consistent with the same westward decreasing trend in the climatological distribution of these low-level clouds [*Deser et al.,* 1993].

4. Atlantic TIWs

An equatorial cold tongue starts to appear in late May, 1999, in the Atlantic. As the equatorial currents and the equatorial SST front start to strengthen, TIWs begin to develop in early June. In the zonal direction, Atlantic TIWs grow their amplitude rapidly from 0° to 10°W, reach maximum magnitude around 15°W and then decay westward (Figure 10). But their propagation can be traced to 40°W. TMI-SSM/I combined wind speed shows similar propagating variability clearly in association with TIWs. Unlike the Pacific, however, the Atlantic cold tongue reaches its maximum strength in early August and then weakens (not shown). So do TIWs. Such a rapid development/decay of the Atlantic cold tongue is a climatological feature of the Atlantic [*Mitchell and Wallace,* 1992]. Its Pacific counterpart has a much gradual developmental characteristics presumably because the Atlantic is more strongly influenced by neighboring continents. We thus choose June 13 to September 2 as the period for our Atlantic analysis. Because the QuikSCAT/SeaWinds data are available only after July 21, our analysis uses only 44-day worth vector wind data.

Figure 11 show the regression maps with the center point at 15°W, 1°N. The wavelength of Atlantic TIWs is about 9° in longitude, slightly shorter than the Pacific ones in 1999. The majority of SST anomalies are tightly confined between the equator and 2°N, but they show some degree of northeastward extension. Despite the relative short record of data, wind velocity regression appears to be quite robust, repeating the same correlation pattern with the SST. As at 105°W, the wind response in the Atlantic is dominated by the meridional component, which is southerly (northerly) over the warm (cold) sector of TIWs. Significant zonal wind variability is also seen north of 2°N. Wind velocity response appears to be correlated with local SST to a large extent, but the deviation from this local adjustment also suggests that there are significant SLP-driven wind anomalies directing from the negative to positive SSTAs.

The WV regressions are comparable in magnitude to the Pacific counterpart, and are roughly in phase with surface wind convergence. Weaker but significant signals are captured by LW regressions, whose phase relation with SST pattern is similar to that in the Pacific as well. These LW anomalies are accompanied by precipitation changes in the ITCZ whose southern boundary is located at 4°N. This more southern position of the Atlantic ITCZ makes it more susceptible to TIWs whose SST variability is trapped largely south of 2°N. West of 25°W, SST waves still persist but with much reduced amplitudes (Figure 10). Nevertheless, LW and precipitation regressions remain strong there (Figure 11). While this may be indicative of a higher sensitivity of deep convection to SST variations over warmer total SSTs, small sample size for the Atlantic regression prevents us from making a certain determination. Longitude-time sections of WV and LW are much more noisy

than in the Pacific, but their co-variability with TIWs is still discernible (not shown). Despite that the same 12° moving average is applied in the zonal direction, a match in dominant wavelength between SST waves and ITCZ variability–9° in the Atlantic vs. 12° in the Pacific–further indicates that the ITCZ response is real.

5. Summary

We have used the newly available high-resolution measurements made by three different types of microwave instruments on board five co-orbiting satellites to study monthly ocean-atmosphere variability in the equatorial Pacific and Atlantic in the second half of 1999, a year of strong TIWs. We apply a simple spatial filter to the data and use the linear regression technique to obtain regional characteristics of TIWs in different longitudinal sectors.

In the far eastern Pacific at 105°W, TIW-induced SST are tightly trapped on the sharp equatorial SST front between the equator and 3°N. Anomalous wind is dominated by its meridional component and correlated with local SST anomaly, a phase relation in support of *Hayes et al.'s* [1989] momentum mixing mechanism. An increase in non-precipitating cloud cover over the troughs of SST waves first reported by *Deser et al.* [1993] based on visible cloud data is also confirmed here by microwave measurements of cloud liquid water and precipitation.

In the central Pacific at 135°W, the equatorial front broadens, and so does the meridional scale of SST waves. A number of significant changes in the spatial structures of atmospheric response are found in our analysis. First, we find evidence for SLP-driven anomalous winds that flow from the cold to warm section of a SST wave and are comparable in magnitude to those due to vertical mixing of momentum. Second, the SST signals south of the equator become more pronounced, inducing much stronger wind response per unit SST change than north of the equator. Third, we detect significant remote response in wind, water vapor, cloud liquid water, and precipitation in the southern portion of the ITCZ where little direct TIW forcing is found. The water vapor, cloud and precipitation changes in the ITCZ appear to be induced by surface wind convergence and are in quadrature with SST waves to the south. Increased convective activity is sandwiched by the ridge of a SST wave to the west and the trough to the east. This TIW-induced ITCZ variability confirms *Xie et al.'s* [1998] hypothesis based on atmospheric GCM results.

TIWs in the Atlantic force an atmospheric response that shares the characteristics with TIWs both in the eastern and central Pacific. As in the far eastern Pacific, its SST signals are tightly trapped within a narrow latitudinal band north of the equator, but they induce significant variations in water vapor and clouds at the ITCZ, which takes a more southern position than the Pacific one.

The global view of ocean-atmospheric variability with TIWs and its regional characteristics are new results from this study. Although TIWs are energetic in the equatorial oceans, their atmospheric response extends farther north and reaches the ITCZ. Anomalous wind velocity has an amplitude of 1-1.5 m/s, or about 15% of the monthly-mean value. In the ITCZ, cloud water variability is 0.03 mm, or 30% of total RMS intra-monthly variance. The precipitation variability is 2.2 mm/day, or 15% of total RMS variance. The zonally repeating, highly coherent patterns from our analysis demonstrate that the current satellite technologies are capable of detecting such subtle low-frequency changes even within the highly variable, noisy ITCZ where synoptic variability in precipitation can be much larger than its monthly mean.

Most of the world ocean is not warm enough to support deep atmospheric convection, where the understanding of ocean-atmosphere interaction we gained from El Niño/Southern Oscillation studies is not directly applicable. Recent studies have revealed large decadal variability in such cold surface oceans such as off-equatorial tropical Atlantic, extratropical North Atlantic and North Pacific. How the atmosphere responds to SST changes is a key to understanding these variabilties. It is extremely difficult to sort out their causality from observations in these regions where local winds are known to be a major cause of SST variability by means of surface heat flux and Ekman advection. TIWs thus offer a rare opportunity for studying atmospheric response to SST variability over cold ocean surface because we know that to the first order, the ocean is driving the atmosphere in this particular phenomenon. Even with this causality known, the rich structures of ocean-atmosphere co-variability–local boundary layer response and remote deep response in the ITCZ–revealed here call for further studies and understanding. Why is the ratio of wind speed to SST anomaly larger south of the equator? What is the mechanism for the deep remote response in the ITCZ? What determines the relative

importance between the vertical mixing and SLP forcing? High-resolution numerical modeling is necessary to fully address these questions, while the regression maps and the regional characters they reveal provide an observational reference to which model results should be compared. Satellite measurements also help to confirm the location of TIW in September 1999 for the cruise of the Japanese research vessel, Shoyo-maru, which conducted a zonal transection of the tropical eastern Pacific to study the TIW [*Shiotani et al.,* 2000]. The preliminary results consisting of composite wind and temperature soundings in the atmospheric boundary layer have been used by *Liu et al.* [2000] to confirm the mixing hypothesis. The coherence between SST and winds above the boundary layer is being examined, using this set of data.

Acknowledgments.

We would like to thank X. Xie for preparing the QuikSCAT/SeaWinds product, and two anonymous reviewers for comments that led to improved presentation. The TMI and SSM/I data are obtained from the web site of Remote Sensing Systems. This study is supported by NASA QuikSCAT (SPX and WTL) and TRMM (WTL) Missions. IPRC contribution number xxx and SOEST contribution number xxx. The IPRC is partly supported by the Frontier Research System for Global Change.

References

Chang, C. P., Westward propagating cloud patterns in the tropical Pacific as seen from time composite satellite photographs, *J. Atmos. Sci., 27,* 133-138, 1970.

Chelton, D. B., F. J. Wentz, C. L. Gentemann, R. A. de Szoeke and M.G. Schlax, Satellite microwave SST observations of transequatorial tropical instability waves, *Geophys. Res. Lett., 27,* 1239-1242, 2000a.

Chelton, D. B., S. K. Esbensen, M. G. Schlax, N. Thum, M. H. Freilich, F. J. Wentz, C. L. Gentemann, M. J. McPhaden and P.S. Schoph, Observations of coupling between surface wind stress and sea surface temperature in the eastern tropical Pacific, *J. Climate,* in press, 2000b.

Chelton, D. B., M. G. Schlax, J. M. Lyman and R. A. de Szoeke, The latitudinal structure of monthly variability in the tropical Pacific, *J. Phys. Oceanogr.,* submitted, 2000c.

Cox, M. D., Generation and propagation of 30-day waves in a numerical model of the Pacific, *J. Phys. Oceanogr., 10,* 1168-1186, 1980.

Deser, C., J. J. Bates and S. Wahl, The influence of sea surface temperature on stratiform cloudiness along the equatorial front in the Pacific ocean, *J. Climate, 6,* 1172-1180, 1993.

Halpern, D., R. A. Knox and D. S. Luther, Observations of 20-day period meridional current oscillations in the upper ocean along the Pacific equator, *J. Phys. Oceanogr., 18,* 1514-1534, 1988.

Hansen, D. V. and C. A. Paul, Genesis and effects of long waves in the equatorial Pacific, *J. Geophys. Res., 89,* 10431-10440, 1984.

Hashizume, H., Response of atmospheric boundary layer to tropical instability waves: Satellite scatterometer data analysis, *M.Sc. Dissertation, Hokkaido Univ., Sapporo, Japan,* 1998.

Hayes, S. P., M. J. McPhaden and J. M. Wallace, The influence of sea surface temperature on surface wind in the eastern equatorial Pacific, *J. Climate, 2,* 1500-1506, 1989.

Lau, K. -H. and N. -C. Lau, Observed structure and propagation characteristics of tropical summertime synoptic scale disturbances, *Mon. Wea. Rev., 118,* 1888-1913, 1990.

Legeckis, R., Long waves in the eastern equatorial Pacific: A view of a geostationary satellite, *Science, 197,* 1177-1181, 1977.

Lindzen, R. S. and S. Nigam, On the role of sea surface temperature gradients in forcing low level winds and convergence in the tropics, *J. Atmos. Sci., 44,* 2418-2436, 1987.

Liu, W. T., X. Xie, P. S. Polito, S. -P. Xie, and H. Hashizume, Atmospheric manifestation of tropical instability waves observed by QuikSCAT and Tropical Rain Measuring Mission, *Geophys. Res. Lett., 27,* 2545-2548, 2000.

Liu, W. T., W. Tang, and P. S. Polito, NASA Scatterometer provides global ocean-surface wind fields with more structures than numerical weather prediction, *Geophys. Res. Lett., 25,* 761-764, 1998.

McPhaden, M., Monthly period oscillations in the Pacific North Equatorial Countercurrent, *J. Geophys. Res., 101,* 6337-6359, 1996.

Mitchell, T. P. and J. M. Wallace, The annual cycle in equatorial convection and sea surface temperature, *J. Climate, 5,* 1140-1156, 1992.

Philander, S. G. H., Instabilities of zonal equatorial currents 2, *J. Geophys. Res., 83,* 3679-3682, 1978.

Raymond, D. J., C. Lopez-Carrillo and L. L. Cavazos, Case-studies of developing east Pacific easterly waves, *Q. J. Roy. Meteor. Soc., 124,* 2005-2034, 1998.

Shibata, A., K. Imaoka, M. Kachi, and H. Murakami, SST observation by TRMM Microwave Imager aboard Tropical Rainfall Measuring Mission (in Japanese), *Umi no Kenkyu, 8,* 135-139, 1999.

Shiotani, M., M. Fujiwara, S. -P. Xie, H. Hashizume, T. Saito, T. Watanabe and F. Hasebe, SOWER/Pacific the Shoyo-maru Pacific ocean-atmospheric survey, *Stratospheric Processes And their Role in Climate (SPARC) Newsletter, 14,* 17-18 and II-III, 2000.

Wallace, J. M., T. P. Mitchell and C. Deser, The influence of sea surface temperature on surface wind in the east-

ern equatorial Pacific: Seasonal and interannual variability, *J. Climate, 2,* 1492-1499, 1989.

Weisberg, R. H., Instability waves observed on the equator in the Atlantic Ocean during 1983, *Geophys. Res. Lett., 11,* 753-756, 1984.

Wentz, F. J., C. Gentemann, D. Smith, and D. Chelton, Satellite measurements of sea surface temperature through clouds, *Science, 288,*847-850, 2000.

Wentz, F. J., A well-calibrated ocean algorithm for special sensor microwave/imager, *J. Geophys. Res., 102,* 8703-8718, 1997.

Xie, S. -P., M. Ishiwatari, H. Hashizume and K. Takeuchi, Coupled ocean-atmospheric waves on the equatorial front, *Geophys. Res. Lett., 25,* 3863-3866, 1998.

Xie, S. -P., Westward propagation of latitudinally asymmetry in a coupled ocean-atmosphere model, *J. Atmos. Sci., 53,* 3236-3250, 1996.

Yu, Z., J. P. McCreary and J. A. Proehl, Meridional asymmetry and energetics of tropical instability waves, *J. Phys. Oceanogr., 25,* 2997-3007, 1995.

H. Hashizume, Graduate School of Environmental Earth Science, Hokkaido University, Sapporo 060-0810, Japan. (e-mail: zume@ees.hokudai.ac.jp)

S.-P. Xie, International Pacific Research Center and Department of Meteorology, University of Hawaii, Honolulu, HI 96822. (e-mail: xie@soest.hawaii.edu)

W.T. Liu, Jet Propulsion Laboratory, Pasadena, CA 91109-8099. (e-mail: liu@pacific.jpl.nasa.gov)

K. Takeuchi, Institute of Low Temperature Science, Hokkaido University, Sapporo 060-0819, Japan. (e-mail: takeuchi@lowtem.hokudai.ac.jp)

Received May 19, 2000; revised October 2, 2000; accepted October 11, 2000.

[1]Graduate School of Environmental Earth Science, Hokkaido University, Sapporo, Japan.

[2]International Pacific Research Center and Department of Meteorology, University of Hawaii, Honolulu, Hawaii.

[3]Jet Propulsion Laboratory, Pasadena, California.

[4]Institute of Low Temperature Science, Hokkaido University, Sapporo, Japan.

This preprint was prepared with AGU's LaTeX macros v5.01. File trmm˙www formatted November 29, 2000.

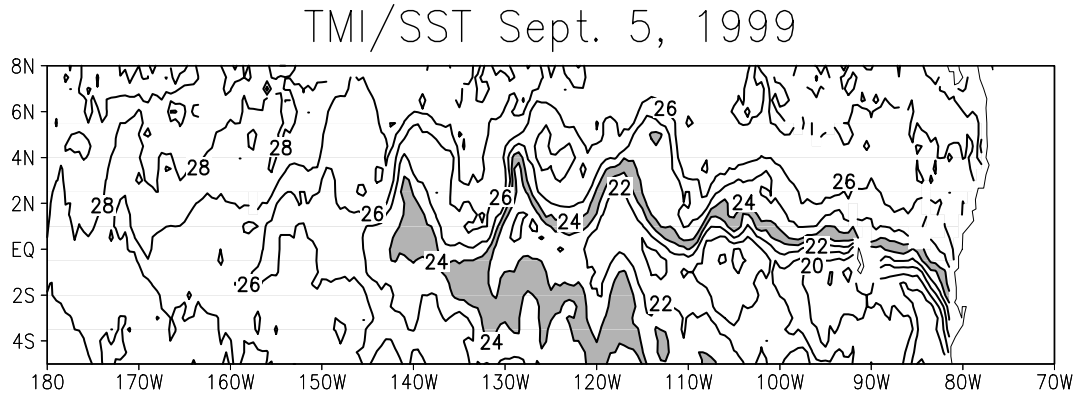

Figure 1. TMI measured SST distribution averaged for September 4-6, 1999.

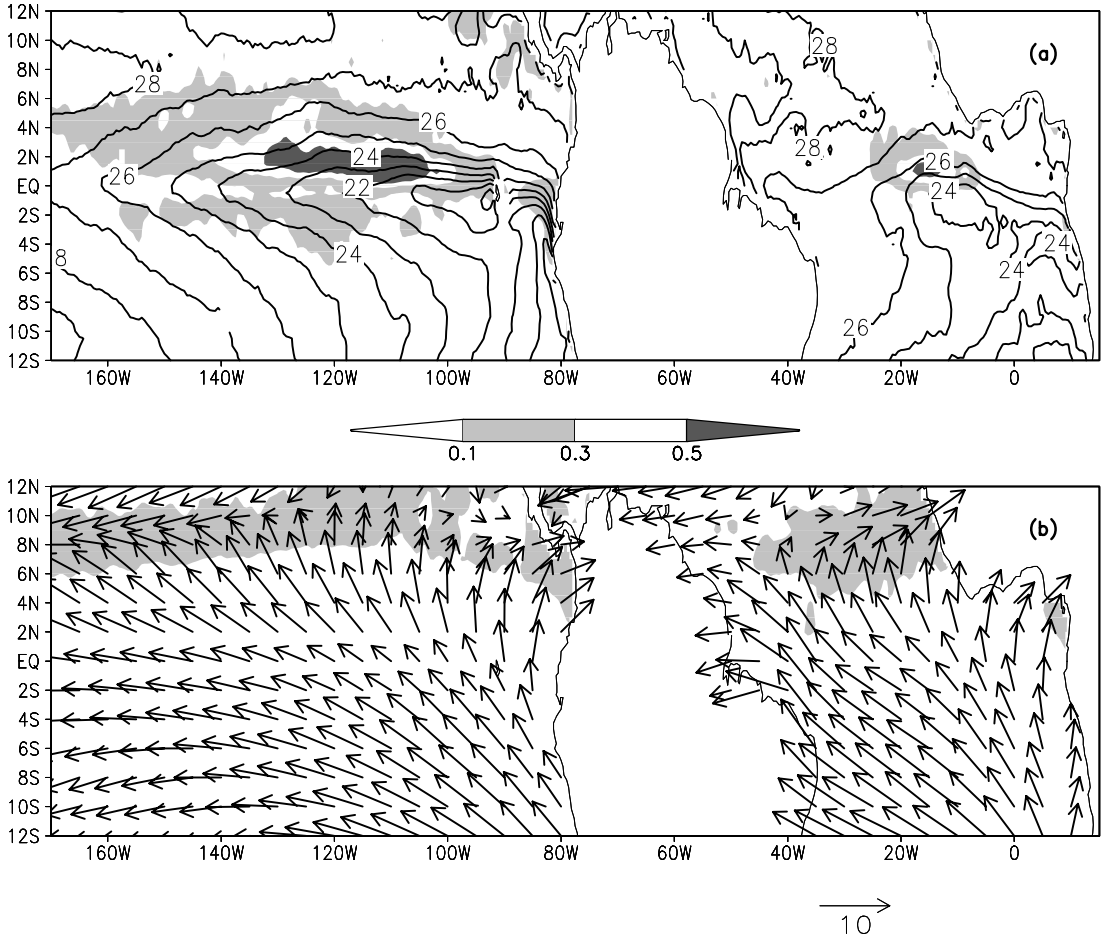

Figure 2. (a) Time average (contours in °C) and variance (shade in $°C^2$) of SST. (b) Mean wind velocity (vectors) and mean precipitation (shade>10 mm/day). Time average is performed for July 21-December 28 for the Pacific, for June 12-September 3 for the Atlantic SST and precipitation, and for July 21-September 3, 1999 for the Atlantic wind velocity.

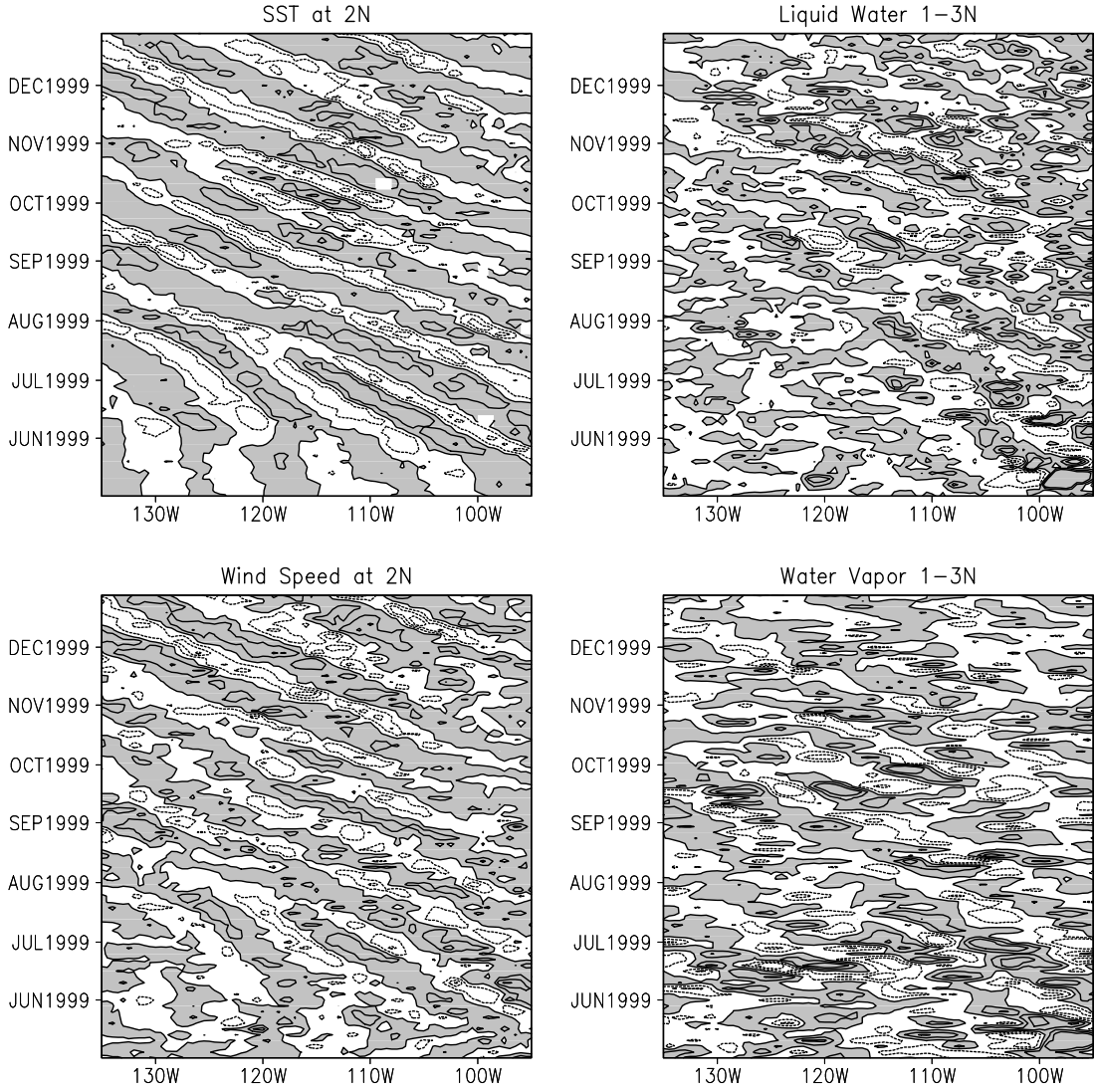

Figure 3. Time-longitude sections of anomalous SST [contour interval (c.i.) = 1 K], wind speed (c.i. = 0.75 m/s) along 2°N, water vapor (c.i. = 1 mm) and cloud liquid water (c.i. = 10^{-2} mm) averaged for 1°N-3°N. Positive values are shaded.

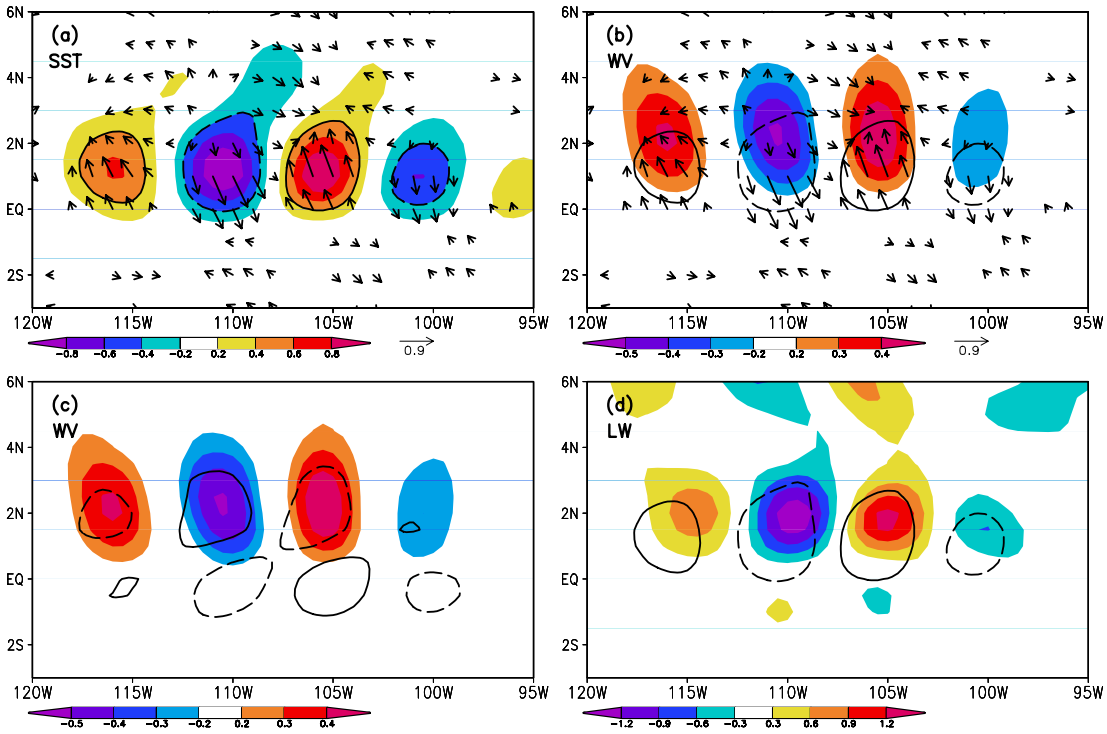

Figure 4. Composite regression pattern with the center point at 105°W, 1°N: (a) SST, (b) water vapor (mm K^{-1}) and wind velocity (m/s K^{-1}), (c) water vapor (mm K^{-1}), and (d) cloud liquid water (10^{-2} mm K^{-1}). The SST = ±0.4 contours are plotted in (a), (b) and (d) to show its centers of action. The wind divergence = $\pm 0.3\times10^{-5}$ s^{-1} K^{-1} contour is plotted in (c).

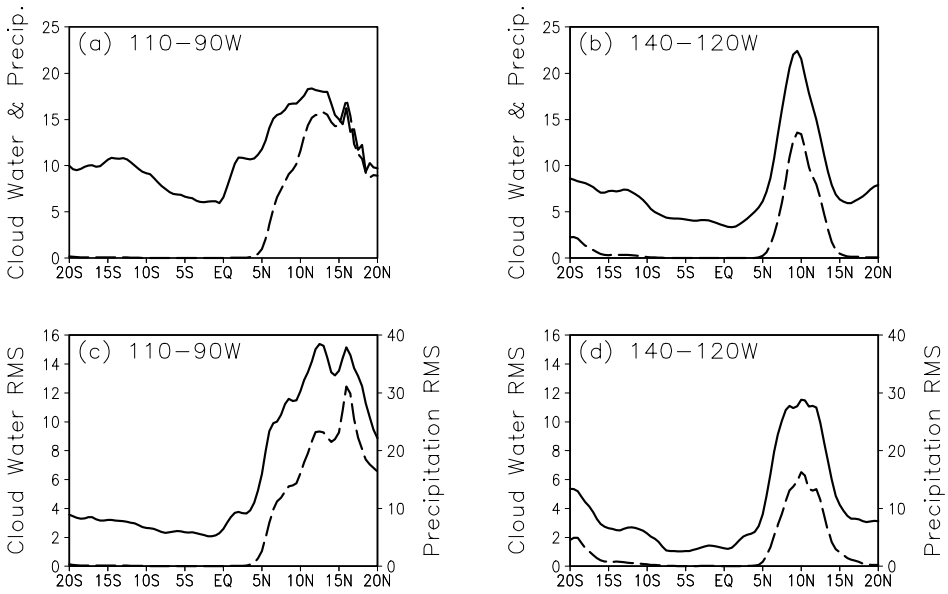

Figure 5. Mean cloud water (10^{-2} mm; solid) and precipitation (mm/day; dashed line) as a function of latitude averaged for (a) 110°W-90°W and (b) 140°W-120°W. The lower panels are for the standard deviation of intra-monthly anomalies, which are defined as the deviation from 30-day running mean.

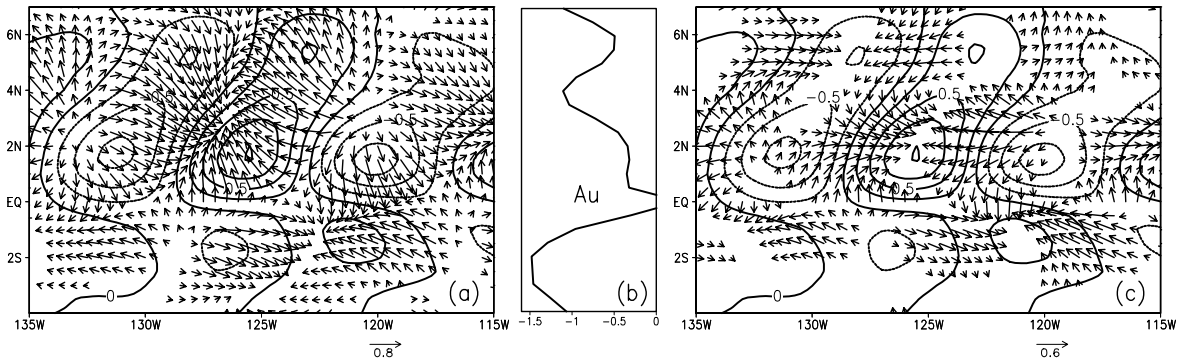

Figure 6. (a) Composite regressions for SST (contours) and wind velocity (vectors) with the center point at 125°W, 2°N. (b) Spatial regression coefficient A_u as a function of latitude. (c) "SLP-driven" anomalous wind velocity, U_p, along with the SST regression pattern.

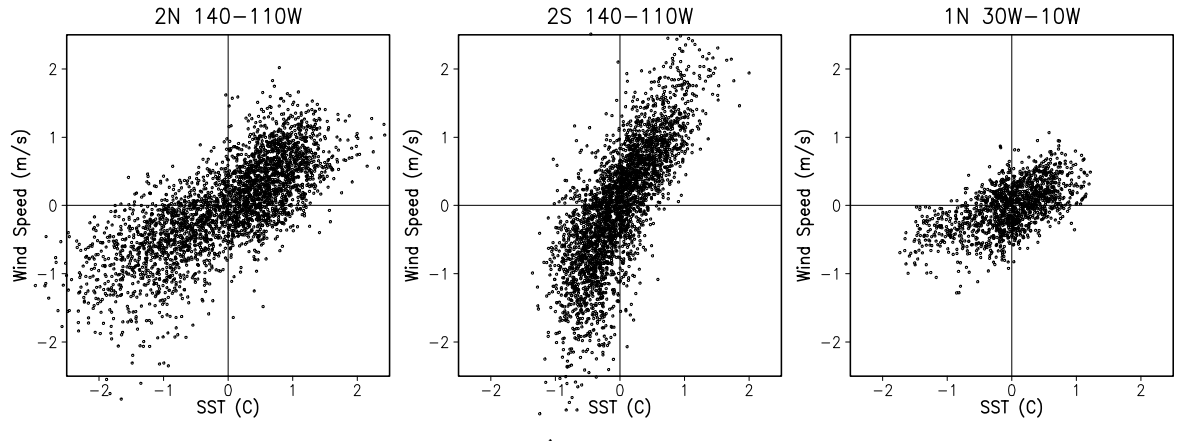

Figure 7. Scatter plots of SST and wind speed in the equatorial North (left) and South (middle) Pacific, and equatorial Atlantic (right).

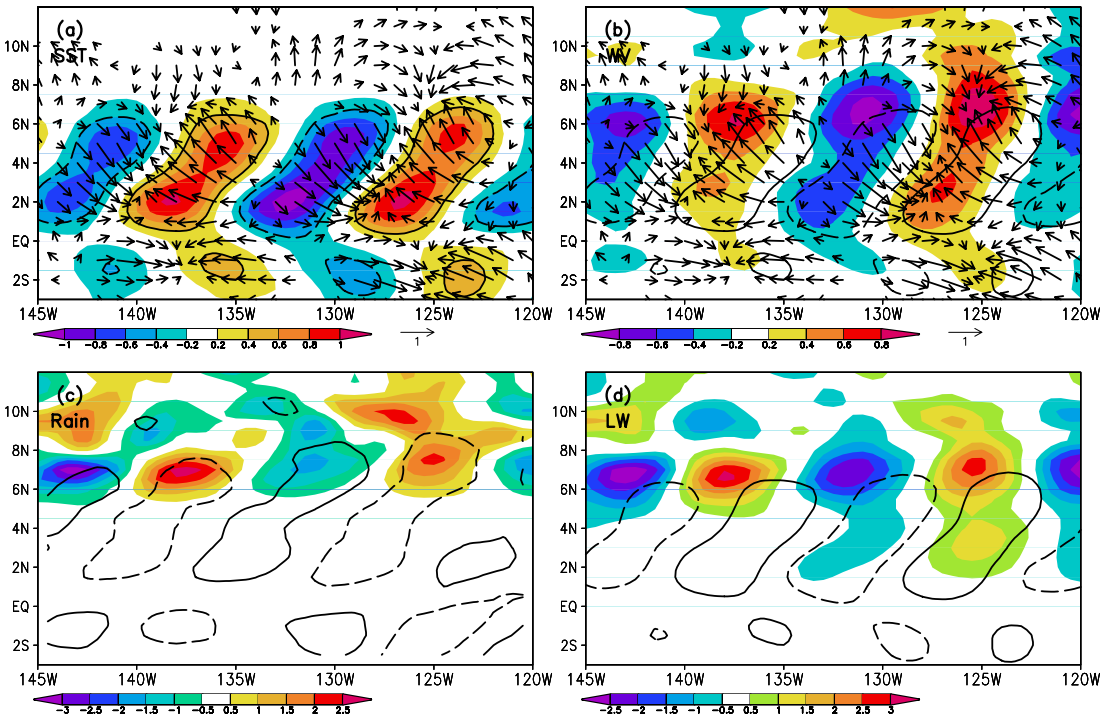

Figure 8. Composite regressions with the center point at 135°W, 5°N for (a) SST, (b) water vapor (mm K^{-1}), (c) precipitation (mm/day K^{-1}) and (d) cloud liquid water (10^{-2} mm K^{-1}). Vectors in (a) and (b) are for wind velocity regressions. The SST = ±0.4 contours are plotted in (a), (b) and (d) to show its centers of action. The wind divergence = $\pm 0.3\times10^{-5}$ s^{-1} K^{-1} contour is plotted in (c).

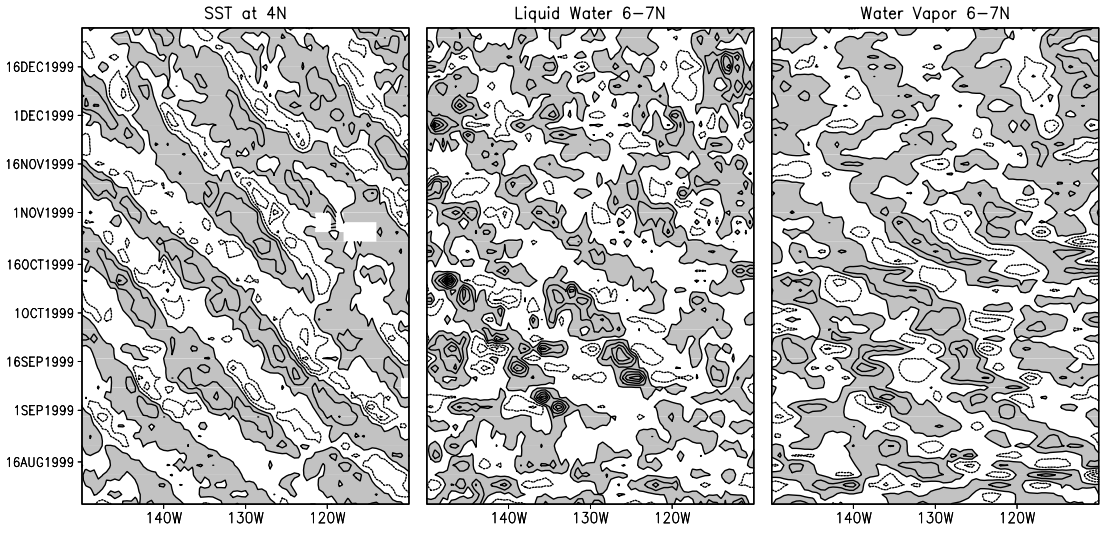

Figure 9. Time-longitude sections of anomalous SST at 4°N (left; c.i. = 0.75 K), cloud liquid water (middle; c.i. = 5×10^{-2} mm) and water vapor (right; c.i. = 1.5 mm) averaged for 6°N-7°N. Positive values are shaded.

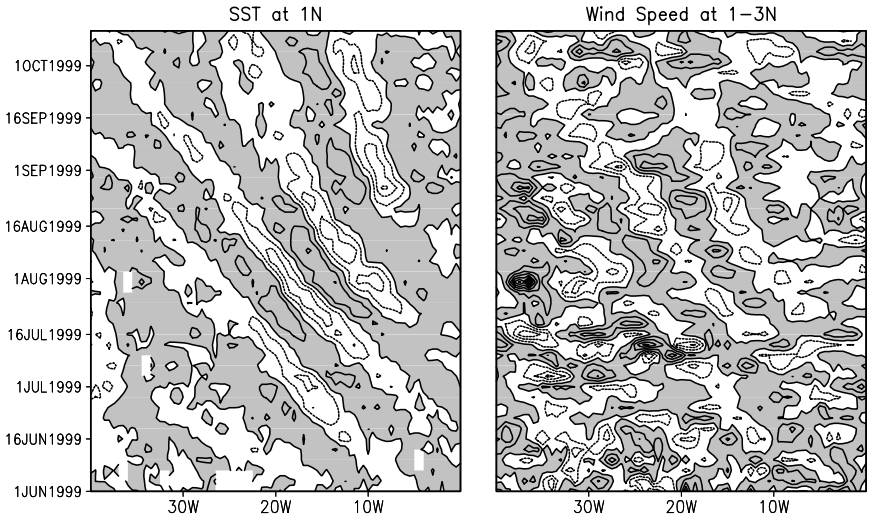

Figure 10. Time-longitude sections of anomalous SST (left; c.i. = 0.75 K) and wind speed (right; c.i. = 0.5 m/s) in the Atlantic sector. Positive values are shaded.

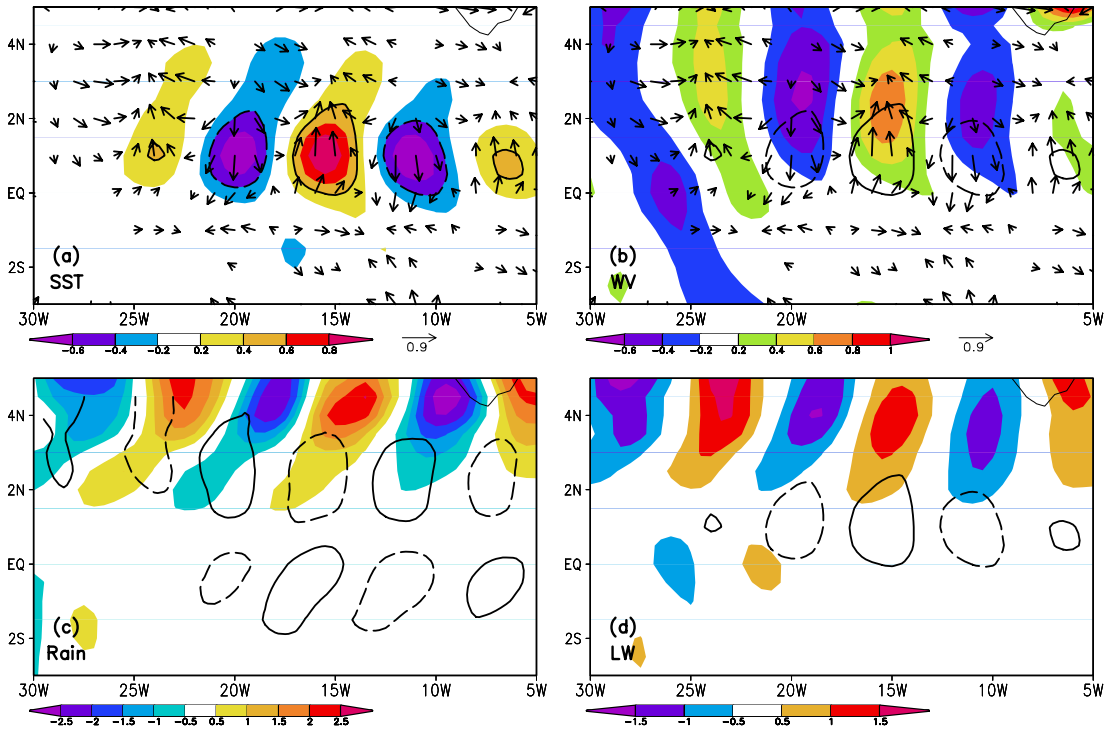

Figure 11. Same as Figure 8 but for the center point at 15°W, 1°N in the Atlantic.